Supplementary Materials

Reaction-anchored generative informatics for million-scale CO_2 catalyst screening via multi-adsorbate constraints

Dongjin Tang[1,2,#], Ruili Li[3,4,#], Zhidi Lei[5], Qingqing Mao[6], Ritankar Das[6], Beien Zhu[1,7], Yi Gao[1,7], Rui Qi[1,7,*]

[1]Photon Science Research Center for Carbon Dioxide, Shanghai Advanced Research Institute, Chinese Academy of Sciences, Shanghai 201210, China.
[2]School of Materials Science and Engineering, Xiangtan University, Xiangtan 411105, Hunan, China.
[3]Key Laboratory of Interfacial Physics and Technology, Shanghai Institute of Applied Physics, Chinese Academy of Sciences, Shanghai 201800, China.
[4]University of Chinese Academy of Sciences, Beijing 100049, China.
[5]Shanghai Synchrotron Radiation Facility, Shanghai Advanced Research Institute, Chinese Academy of Sciences, Shanghai 201204, China.
[6]Titan Holdings, Hayward, CA 94541, USA.
[7]State Key Laboratory of Low Carbon Catalysis and Carbon Dioxide Utilization, Shanghai Advanced Research Institute, Chinese Academy of Sciences, Shanghai 201210, China.
[#]These authors contributed equally to this work.

***Correspondence to:** Dr. Rui Qi, Photon Science Research Center for Carbon Dioxide, Shanghai Advanced Research Institute, Chinese Academy of Sciences, Shanghai 201210, China. E-mail: qir@sari.ac.cn

Supplementary Methods

UMA-based structural representation and geometry optimization

Structural representations and geometry optimizations were performed with the pretrained UMA uma-s-1p2 checkpoint under the OC20 task setting[1,2]. UMA employs an equivariant spherical-channel network. For each atom, the final layer-normalized node representation was extracted from the UMA backbone before the energy and force prediction heads. The rotationally invariant $\ell = 0$ scalar component was retained as a 128-dimensional atomic embedding:

$$\mathbf{h}_i \in \mathbb{R}^{128} \tag{S1}$$

where i denotes the atom index.

Two complementary structural descriptors were constructed from these atomic embeddings. To characterize the overall chemical and structural environment of each surface configuration s, the $\ell = 0$ scalar embeddings of all non-adsorbate atoms were mean-pooled as:

$$\mathbf{g}_s = \frac{1}{|\mathcal{I}_s|}\sum_{i\in\mathcal{I}_s}\mathbf{h}_i \in \mathbb{R}^{128} \tag{S2}$$

where $\mathcal{I}_s$ denotes the set of non-adsorbate atoms in configuration s, and $|\mathcal{I}_s|$ is its cardinality. The resulting substrate-level descriptor $\mathbf{g}_s$ was used to characterize the global structural distribution of the generated surface space.

For the local adsorption environment used in subsequent clustering, the $\ell = 0$ scalar embedding of the surface-anchoring ethoxy O atom was retained without pooling:

$$\mathbf{o}_s = \mathbf{h}_{i_{\mathrm{O,anch}}(s)} \in \mathbb{R}^{128} \tag{S3}$$

Here, $i_{\mathrm{O,anch}}(s)$ denotes the atom index of the ethoxy O atom directly associated with the surface adsorption site. The local descriptor $\mathbf{o}_s$ was used for clustering, representative sampling, and subsequent neighborhood expansion.

Representative *OCH_2CH_3 configurations and their corresponding bare slabs were optimized with the same UMA model using batched L-BFGS. Atoms designated as fixed in the input slab model remained constrained, while all other surface and adsorbate atoms were relaxed. Optimizations were terminated when the maximum force on unconstrained

atoms fell below 0.05 eV $Å^{-1}$ or when 500 ionic steps had been reached. To construct *CO and *H inputs, ethoxy was removed from the relaxed *OCH_2CH_3 structure and the in-plane coordinates of the original anchoring O atom were retained as the initial lateral adsorption position. For *CO, the C atom was placed at this lateral position and its height was adjusted to give an initial 2.2 Å distance from the nearest relax-able surface atom; the O atom was placed 1.128 Å above C along the surface normal. For *H, the initial H-surface distance was 2.0 Å. If the retained lateral coordinate lay outside the corresponding distance sphere of the nearest surface atom, C and H were instead initialized directly above that atom using vertical offsets of 2.0 and 1.6 Å, respectively. These placements defined only the initial configurations; no adsorbate coordinate was constrained during subsequent relaxation. The resulting UMA-relaxed structures were then converted into VASP input geometries while preserving the simulation cell, atomic species, coordinates, and fixed-atom constraints defined for the slab. The corresponding scripts are available at https://github.com/torenyx/uma-structure-tools.

Adsorption energies were evaluated using a method-consistent implementation of the OC20 stoichiometric referencing scheme[1]:

$$\Delta E_{\text{ads}} = E_{\text{sys}} - E_{\text{slab}} - E_{\text{ref}} \tag{S4}$$

where E_{sys} and E_{slab} denote the energies of the relaxed adsorbate-slab system and the corresponding relaxed bare slab for configuration i, respectively. E_{ref} is the reference energy of adsorbate.

The elemental reference energies for H, O, and C were constructed from H_2, H_2O, and CO following the OC20 stoichiometric relations:

$$\mu_H = \frac{1}{2}E(\mathrm{H_2}) \tag{S5}$$

$$\mu_O = E(\mathrm{H_2O}) - E(\mathrm{H_2}) \tag{S6}$$

$$\mu_C = E(\mathrm{CO}) - E(\mathrm{H_2O}) + E(\mathrm{H_2}) \tag{S7}$$

$$E_{ref}(X) = \sum_{\alpha \in \{\mathrm{C,H,O}\}} n_\alpha(X)\mu_\alpha \tag{S8}$$

In Supplementary Equations (S5)–(S7), $E(\mathrm{H_2})$, $E(\mathrm{H_2O})$, and $E(\mathrm{CO})$ are the isolated-

molecule energies, and μ_α is the corresponding elemental reference energy for element α. In Supplementary Equation (S8), $n_\alpha(X)$ is the number of atoms of element $\alpha \in \{C,H,O\}$ in adsorbate X. UMA and DFT use the same stoichiometric reference construction, while the numerical reference energies are method-specific. The UMA molecular energies were evaluated with the same uma-s-1p2 checkpoint and OC20 task setting used for the surface calculations.

The resulting UMA elemental reference energies were −7.29 eV for C, −3.47 eV for H, and −7.21 eV for O. Accordingly, the adsorbate reference energies used for adsorption-energy evaluation were −39.13 eV for OCH_2CH_3, −14.50 eV for CO, and −3.47 eV for H. These values were evaluated from the unrounded molecular energies; the elemental reference energies are reported here to three decimal places. These reference energies were used consistently in all reported UMA adsorption-energy calculations.

DFT calculations

Spin-polarized DFT calculations were performed using VASP[3,4]. Exchange-correlation interactions were described using the RPBE functional[5], and core-valence interactions were treated using PAW-PBE potentials[6]. The generated slabs retained their original simulation cells with vacuum regions exceeding 15 Å along the surface-normal direction, without imposing a common Bravais lattice. Because the generated slab structures are not derived from uniquely assigned parent bulk phases, bulk space groups, lattice parameters, and Miller indices cannot be unambiguously assigned to the 75 composition-level candidates. Slab atoms within 2.0 Å below the uppermost slab atom were relaxed, whereas deeper slab atoms were fixed; all adsorbate atoms were fully relaxed. Reciprocal-space integration used the same Γ-centered k-point construction as described in the main-text Methods. Geometry optimizations were converged to a maximum residual force of 0.05 eV $Å^{-1}$ and an electronic self-consistency threshold of 1×10^{-4} eV, with up to 60 electronic iterations per SCF cycle and 2,000 ionic steps. No element-specific initial magnetic moments were assigned, and VASP's default initial value of 1 μB per atom was used. No independent charge-density or potential cutoff was specified beyond the standard PAW and plane-wave settings. Adsorption energies were evaluated with the same stoichiometric reference construction as Supplementary Equation (S4), using method-specific reference energies. The reported adsorption energies correspond to the 0 K electronic-energy limit; zero-point-energy, enthalpic, and

entropic corrections were not included. The transition state was located using the dimer method in VASP[7,8]. Vibrational frequency analysis was subsequently performed to confirm the transition-state character, with each transition state exhibiting a single imaginary frequency along the reaction coordinate. The activation barrier was calculated as:

$$E_{\mathrm{a}}=E_{\mathrm{TS}}-E_{\mathrm{IS}} \tag{S9}$$

Subsequent electronic-structure analyses were performed on the DFT-relaxed geometries within the same RPBE-PAW framework, using an electronic self-consistency threshold of 1×10^{-6} eV. Static charge-density calculations used the corresponding Γ-centered k-point meshes, while PDOS calculations employed a sampling-length parameter of 60 Å, a 3,001-point energy grid, and the tetrahedron method with Blöchl corrections[9].

Charge redistribution upon adsorption was evaluated from the electron-density difference:

$$\Delta\rho(\mathbf{r}) = \rho_{\mathrm{slab}+X}(\mathbf{r}) - \rho_{\mathrm{slab}}(\mathbf{r}) - \rho_{X}(\mathbf{r}) \tag{S10}$$

Here, the three terms denote the electron densities of the adsorbate-slab system, the corresponding slab, and the isolated adsorbate X, respectively, all evaluated in the same periodic cell with identical k-point and FFT grids. Positive and negative density differences indicate electron accumulation and depletion, respectively, and the resulting isosurfaces were visualized using VESTA[10].

Clustering

Clustering was performed in the 128-dimensional O-centered embedding space defined in Supplementary Equation (S3). For each *OCH_2CH_3 adsorption configuration indexed by s, $\mathbf{o}_s$ denotes the 128-dimensional scalar embedding of the surface-anchoring ethoxy O atom. A total of $N = 839{,}237$ embeddings were included. To remove the common offset of the embedding space, the global mean vector was calculated as:

$$\mathbf{m}_o = \frac{1}{N}\sum_{s=1}^{N}\mathbf{o}_s \tag{S11}$$

Each mean-centered embedding was subsequently normalized to unit Euclidean norm:

$$\tilde{\mathbf{o}}_s = \frac{\mathbf{o}_s - \mathbf{m}_o}{\|\mathbf{o}_s - \mathbf{m}_o\|_2} \tag{S12}$$

Here, $\mathbf{m}_o$ is the global mean vector, $\tilde{\mathbf{o}}_s$ is the centered and unit-normalized embedding of configuration s, and $\|\cdot\|_2$ denotes the Euclidean norm. The inner product between any two processed embeddings is therefore equal to their cosine similarity.

The normalized embeddings were partitioned using GPU-accelerated spherical k-means implemented in Faiss[11]. Unit-norm centroids $\mathbf{c}_k \in \mathbb{R}^{128}$ were optimized by maximizing the total cosine similarity over a training subset:

$$\max_{\{\mathbf{c}_k\}_{k=1}^{K}} \sum_{s\in\Omega} \max_{1\le k\le K} \tilde{\mathbf{o}}_s^{\top}\mathbf{c}_k \tag{S13}$$

subject to

$$\mathbf{c}_k \in \mathbb{R}^{128}, \quad \|\mathbf{c}_k\|_2 = 1, \quad k = 1, \ldots, K \tag{S14}$$

where $K = 2{,}000$ is the number of clusters, k indexes clusters, Ω is the index set used for centroid optimization, and $(\cdot)^{\top}$ denotes transpose. Under the Faiss default cap of 256 training vectors per centroid, 512,000 embeddings were sampled from the complete dataset for centroid estimation. Optimization was performed for 25 iterations from five independent initializations with a random seed of 42, and the solution with the highest final objective value was retained.

After centroid optimization, all 839,237 embeddings were assigned by exact inner-product search to the centroid with the highest cosine similarity:

$$z_s = \arg\max_{1\le k\le K} \tilde{\mathbf{o}}_s^{\top}\mathbf{c}_k \tag{S15}$$

where z_s is the cluster assignment of configuration s. Its similarity to the assigned centroid was recorded as:

$$\rho_s = \tilde{\mathbf{o}}_s^{\top}\mathbf{c}_{z_s} \tag{S16}$$

where ρ_s is the corresponding cosine similarity. To obtain a compact yet structurally diverse representative set, five structures were selected from each cluster according to the 0th, 25th, 50th, 75th, and 95th percentiles of the cluster-specific centroid-similarity distribution. For each target percentile, the structure whose ρ_s value was closest to the

corresponding percentile value was retained, yielding 10,000 representative *OCH_2CH_3 configurations in total for subsequent UMA-based adsorption-energy evaluation.

Geometric deduplication

Geometric deduplication was performed on the relaxed *OCH_2CH_3 adsorption structures for which the adsorption-energy calculations of *OCH_2CH_3, *CO, and *H had converged. Because the corresponding *CO and *H configurations were derived from the same local adsorption environment of each parent *OCH_2CH_3 structure, the relaxed *OCH_2CH_3 configuration was used as the structural identifier for deduplication. Structures were first grouped according to their constituent element sets and then converted from ASE Atoms objects into pymatgen Structure objects using AseAtomsAdaptor. Within each element-set group, geometrically equivalent structures were identified using the StructureMatcher implementation in pymatgen[12]. Matching was performed with the default tolerances of ltol = 0.2, stol = 0.3, and an angular tolerance of 5°, while preserving atomic species during structure mapping. Structures judged equivalent under these criteria were assigned to the same equivalence group, and one representative structure was retained from each group.

Subgroup discovery

Subgroup discovery was applied to the geometrically deduplicated candidate pool to identify compact combinations of elemental properties that enrich structures satisfying all three adsorption-energy criteria[13,14]. The source pool comprised 4,786 unique adsorption structures. Because a fixed descriptor representation was required for each compositional dimensionality, binary and ternary structures were analyzed independently, comprising 3,613 and 928 structures, respectively. Unary and quaternary structures were not included in these searches. Positive and negative labels were assigned according to the joint *OCH_2CH_3/CO/H adsorption-energy criteria prior to elemental safety filtering. Each adsorption structure indexed by i was assigned a binary target label according to:

$$y_i = \begin{cases} 1, \text{if } -4.2 \le \Delta E_{\mathrm{ads},i}^{(\mathrm{UMA})}(*\mathrm{OCH_2CH_3}) \le -3.3, \\ \quad \text{and } -1.0 \le \Delta E_{\mathrm{ads},i}^{(\mathrm{UMA})}(*\mathrm{CO}) \le -0.35, \\ \quad \text{and } \Delta E_{\mathrm{ads},i}^{(\mathrm{UMA})}(*\mathrm{H}) > -0.2, \\ 0, \text{otherwise.} \end{cases} \tag{S17}$$

Thus, $y_i = 1$ if and only if the ethoxy and CO adsorption energies lie within the specified closed intervals and the H adsorption energy is greater than −0.2 eV; otherwise, $y_i = 0$.

The three adsorption-energy constraints are imposed simultaneously.

For each structure, the constituent elements were ordered by increasing atomic number to define reproducible element positions $r = 1, ..., q$, where $q = 2$ and $q = 3$ for the binary and ternary searches, respectively. Each element position was characterized by nine intrinsic elemental properties: atomic radius (R), electron affinity (EA), ionization potential (IP), cohesive energy (EC), number of d-valence electrons (Nd), number of group valence electrons (Nv), electronegativity (EN), Mendeleev number (MN), and relative atomic mass (M). This representation yielded 18 descriptors for each binary structure and 27 descriptors for each ternary structure. Descriptor labels were written as indivisible upright strings, with the terminal numeral directly identifying the element position in the atomic-number ordering; for example, MN1 and Nd2 denote the Mendeleev number of the first element and the number of d-valence electrons of the second element, respectively. The numeral is a position label rather than a crystallographic atomic-site index.

The searches were performed using pysubgroup version 0.9.0 and its beam-search implementation[14]. Numerical selectors were constructed using five-bin equal-frequency discretization. Descriptors containing more than five distinct values were represented by interval selectors defined by the corresponding equal-frequency cut points, whereas descriptors containing no more than five distinct values were represented by equality selectors. A subgroup was defined as the conjunction of at most five selector conditions. The beam width and preliminary result-set size were both set to 200. Minimum subgroup supports of eight and five structures were imposed for the binary and ternary searches, respectively. Following the search, rules were retained only if they contained at least one descriptor associated with each element position, ensuring that the resulting rules reflected contributions from all constituent elements rather than being dominated by a single component. Up to 30 highest-ranked rules were retained for subsequent analysis.

Subgroups were ranked using the StandardQF quality function with exponent $a = 0.5$:

$$Q(S) = \left(\frac{n_S}{N}\right)^a (p_S - p_0), \quad a = 0.5 \tag{S18}$$

where N is the total number of structures in the corresponding binary or ternary dataset, n_S is the number of structures covered by subgroup S, p_S is the positive fraction within S, and p_0 is the positive fraction in the complete dataset. This quality function rewards

positive-class enrichment while penalizing rules with very limited coverage. For each retained rule, the subgroup size, number of covered positive structures, subgroup positive fraction, baseline positive fraction, and enrichment factor were calculated. For $p_0 > 0$, the enrichment factor was defined as:

$$\mathrm{EF}(S) = \frac{p_S}{p_0} \tag{S19}$$

An exact condition-level Shapley decomposition was subsequently applied to the highest-ranked binary and ternary rules to quantify the contribution of each condition to the rule quality[15]. For a rule containing the condition set $\mathcal{C} = \{c_1, ..., c_m\}$, all 2^m possible condition subsets were enumerated. For each coalition $\mathcal{A} \subseteq \mathcal{C}$, subgroup $S_{\mathcal{A}}$ was defined by the conjunction of all conditions in $\mathcal{A}$, and its StandardQF score was used as the characteristic-function value:

$$v(\mathcal{A}) = Q(S_{\mathcal{A}}) \tag{S20}$$

The Shapley contribution of condition c_j was calculated from its weighted marginal contribution over all coalitions that do not contain c_j:

$$\phi_j = \sum_{\mathcal{A} \subseteq \mathcal{C}:\, c_j \notin \mathcal{A}} \frac{|\mathcal{A}|!\ (m - |\mathcal{A}| - 1)!}{m!} \left[v\left(\mathcal{A} \cup \{c_j\}\right) - v(\mathcal{A}) \right] \tag{S21}$$

where $|\mathcal{A}|$ is the number of conditions in coalition $\mathcal{A}$, and m is the total number of conditions in the complete rule. The factorial term weights each marginal contribution according to coalition size. The empty coalition represents the complete dataset and therefore has $v(\emptyset) = 0$. The resulting condition contributions satisfy the efficiency relation:

$$\sum_{j=1}^{m} \phi_j = v(\mathcal{C}) - v(\emptyset) = Q(S_{\mathcal{C}}) \tag{S22}$$

With the condition sets of the selected top rules held fixed, uncertainty in the Shapley contributions was estimated using 2,000 nonparametric bootstrap replicates generated by resampling structures with replacement. For each replicate, all coalition-specific StandardQF scores and the corresponding Shapley contributions were recalculated, and 95% confidence intervals were obtained from the 2.5th and 97.5th percentiles of the bootstrap distributions.

Supplementary Table 1. CPU and GPU wall-clock times for UMA and VASP geometry optimizations

Benchmark	CPU setup	GPU setup	CPU time (min)	GPU time (min)	Speed-up
UMA (72 structures)	32 CPU cores	1 RTX 4090 GPU	163.4	1.25	131×
VASP: Cu–Zn–Rh	32 MPI ranks	2 MPI ranks + 1 RTX 3090 GPU	8.49	39.93	0.213×
VASP: Al–Cu–Pd	32 MPI ranks	2 MPI ranks + 1 RTX 3090 GPU	51.63	108.03	0.478×

Supplementary Table 2. Elemental descriptors used for binary and ternary subgroup discovery.

Descriptor	Definition and unit
R_j	Atomic radius of element *j* (Å)
EA_j	Electron affinity of element *j* (eV)
IP_j	Ionization potential of element *j* (eV)
EC_j	Cohesive energy of element *j* (eV atom^{-1})
Nd_j	Number of d-valence electrons of element *j*
Nv_j	Number of group valence electrons of element *j*
EN_j	Pauling electronegativity of element *j*
MN_j	Mendeleev number of element *j*
M_j	Relative atomic mass of element *j*

Note: Here, $j = 1, 2$ for binary structures and $j = 1, 2, 3$ for ternary structures. Constituent elements were indexed in increasing order of atomic number. The terminal numeral denotes the element position rather than a crystallographic site; for example, MN3 is the Mendeleev number of the third element.

Supplementary Table 3. Chemical systems retained after adsorption-energy screening.

Chemical system		
Cu	Al–Cu	Al–Mn
Al–Pd	Al–Pt	Ca–Bi
Ca–Cu	Cl–Cu	Cu–Ag
Cu–Au	Cu–Ge	Cu–Pt
Cu–Sb	Cu–Y	Cu–Zn
Ga–Hf	Ga–Pt	Mo–Rh
N–Mn	N–V	P–Cr
P–Sc	Ru–In	S–Cr
S–Cu	S–Ni	S–Pd
Sc–Au	Sc–Cu	Sc–In
Sc–Pd	Sc–Zn	Si–Cu
Si–Ni	Te–Ta	Ti–Pd
V–Te	Zn–Pd	Zn–Pt
Zn–Rh	Al–Cu–Pd	Al–Cu–Zn
Al–Ru–Ta	C–V–Ga	Co–Se–Ag
Cu–Ga–Pd	Cu–Pd–Sn	Cu–Rh–Hf
Cu–Y–Sn	Cu–Zn–Au	Cu–Zn–Ir
Cu–Zn–Rh	Ga–Zr–Pd	K–Cu–Sb
Mn–Se–Y	N–Ca–Cr	N–Ca–Ge
N–Ti–Y	Na–Pd–In	Ni–Ga–Nb
P–Sr–Au	S–Se–Mo	S–Ti–Y
Sc–Cu–Ga	Sc–Cu–Pt	Sc–Cu–Zn
Sc–Pd–Hf	Sc–Pd–Ir	Sc–Ru–Sn
Si–Co–Zr	Si–Sc–Cu	Y–Pd–In
Zn–Pd–In	Zn–Pd–Pt	Zn–Y–Pd

Supplementary Table 4. Experimental synthesis precedents for 72 final candidates.

Representative candidates	Experimental synthesis precedent	Representative reference
Cu	Yes	[16]
Al–Cu	Yes	[17]
Al–Mn	Yes	[18]
Al–Pd	Yes	[19]
Al–Pt	Yes	[20]
Ca–Bi	Yes	[21]
Ca–Cu	Yes	[22]
Cl–Cu	Yes	[23]
Cu–Ag	Yes	[24]
Cu–Au	Yes	[25]
Cu–Ge	Yes	[26]
Cu–Pt	Yes	[27]
Cu–Sb	Yes	[28]
Cu–Y	Yes	[29]
Cu–Zn	Yes	[30]
Ga–Hf	Yes	[31]
Ga–Pt	Yes	[32]
Mo–Rh	Yes	[33]
N–Mn	Yes	[34]
N–V	Yes	[35]
P–Cr	Yes	[36]
P–Sc	Yes	[37]
Ru–In	Yes	[38]
S–Cr	Yes	[39]
S–Cu	Yes	[40]
S–Ni	Yes	[41]

Representative candidates	Experimental synthesis precedent	Representative reference
S–Pd	Yes	[42]
Sc–Au	Yes	[43]
Sc–Cu	Yes	[44]
Sc–In	Yes	[45]
Sc–Pd	Yes	[46]
Sc–Zn	Yes	[47]
Si–Cu	Yes	[48]
Si–Ni	Yes	[49]
Te–Ta	Yes	[50]
Ti–Pd	Yes	[51]
V–Te	Yes	[52]
Zn–Pd	Yes	[53]
Zn–Pt	Yes	[54]
Zn–Rh	Yes	[55]
Al–Cu–Pd	Yes	[56]
Al–Cu–Zn	Yes	[57]
Al–Ru–Ta	Yes	[58]
C–V–Ga	Yes	[59]
Co–Se–Ag	Yes	[60]
Cu–Ga–Pd	Yes	[61]
Cu–Pd–Sn	Yes	[62]
Cu–Rh–Hf	Yes	[63]
Cu–Y–Sn	Yes	[64]
Cu–Zn–Au	Yes	[65]
Cu–Zn–Ir	Yes	[66]
Cu–Zn–Rh	Yes	[67]
Ga–Zr–Pd	Yes	[68]

Representative candidates	Experimental synthesis precedent	Representative reference
K–Cu–Sb	Yes	[69]
Mn–Se–Y	Yes	[70]
N–Ca–Cr	Yes	[71]
N–Ca–Ge	Yes	[72]
N–Ti–Y	Yes	[73]
Ni–Ga–Nb	Yes	[74]
P–Sr–Au	Yes	[75]
S–Se–Mo	Yes	[76]
Sc–Cu–Ga	Yes	[77]
Sc–Cu–Pt	Yes	[78]
Sc–Cu–Zn	Yes	[79]
Sc–Pd–Ir	Yes	[80]
Sc–Ru–Sn	Yes	[81]
Si–Co–Zr	Yes	[82]
Si–Sc–Cu	Yes	[83]
Y–Pd–In	Yes	[84]
Zn–Pd–In	Yes	[85]
Zn–Pd–Pt	Yes	[86]
Zn–Y–Pd	Yes	[87]

Supplementary Table 5. Thermodynamic accessibility of 3 candidates without experimental synthesis records.

Representative candidates	E_{form} (eV atom^{-1})	E_{hull} (eV atom^{-1})
Na–Pd–In	−0.38	0.029
S–Ti–Y	−1.85	0.088
Sc–Pd–Hf	2.12	2.925

Note: Thermodynamic data were retrieved from the Materials Project[88]. E_{form} and E_{hull} denote the formation energy per atom and energy above the convex hull per atom, respectively. Structures with $E_{hull} \leqslant 0.10$ eV/atom were regarded as thermodynamically stable or moderately metastable candidates with plausible synthesizability.

Supplementary Table 6. UMA and DFT adsorption energies including *OCH_2CH_3, *CO and *H for the 20 representative candidates.

Representative candidates	Adsorbate	E_{ads}^{UMA} (eV)	E_{ads}^{DFT} (eV)
Al–Cu	*OCH_2CH_3	−3.681	−3.567
Al–Cu	*CO	−0.697	−0.675
Al–Cu	*H	0.041	0.050
Al–Cu–Pd	*OCH_2CH_3	−3.310	−3.256
Al–Cu–Pd	*CO	−0.545	−0.529
Al–Cu–Pd	*H	0.041	0.063
Cu–Zn–Au	*OCH_2CH_3	−3.772	−3.757
Cu–Zn–Au	*CO	−0.513	−0.526
Cu–Zn–Au	*H	0.107	0.119
Cu	*OCH_2CH_3	−3.615	−3.577
Cu	*CO	−0.595	−0.617
Cu	*H	−0.035	−0.023
Al–Cu–Zn	*OCH_2CH_3	−3.749	−3.550
Al–Cu–Zn	*CO	−0.697	−0.638
Al–Cu–Zn	*H	0.073	0.158
Cu–Ga–Pd	*OCH_2CH_3	−4.057	−4.006
Cu–Ga–Pd	*CO	−0.741	−0.752
Cu–Ga–Pd	*H	0.243	0.240
Cu–Zn	*OCH_2CH_3	−3.783	−3.812
Cu–Zn	*CO	−0.680	−0.721
Cu–Zn	*H	0.277	0.261
Sc–Cu–Ga	*OCH_2CH_3	−3.326	−3.329
Sc–Cu–Ga	*CO	−0.728	−0.786
Sc–Cu–Ga	*H	0.420	0.410
Cu–Pd–Sn	*OCH_2CH_3	−3.533	−3.482
Cu–Pd–Sn	*CO	−0.780	−0.827
Cu–Pd–Sn	*H	0.408	0.427
Cu–Zn–Rh	*OCH_2CH_3	−3.443	−3.443
Cu–Zn–Rh	*CO	−0.712	−0.750
Cu–Zn–Rh	*H	0.366	0.334

Representative candidates	Adsorbate	E_{ads}^{UMA} (eV)	E_{ads}^{DFT} (eV)
Sc–Cu–Zn	*OCH_2CH_3	−3.545	−3.533
Sc–Cu–Zn	*CO	−0.619	−0.649
Sc–Cu–Zn	*H	0.354	0.369
Cu–Y–Sn	*OCH_2CH_3	−3.683	−3.577
Cu–Y–Sn	*CO	−0.695	−0.700
Cu–Y–Sn	*H	0.181	0.200
Ga–Hf	*OCH_2CH_3	−3.814	−3.781
Ga–Hf	*CO	−0.409	−0.444
Ga–Hf	*H	−0.011	−0.075
Ga–Pt	*OCH_2CH_3	−3.685	−3.719
Ga–Pt	*CO	−0.568	−0.583
Ga–Pt	*H	0.117	0.143
Ni–Ga–Nb	*OCH_2CH_3	−3.702	−3.665
Ni–Ga–Nb	*CO	−0.974	−0.888
Ni–Ga–Nb	*H	0.339	0.405
Sc–Au	*OCH_2CH_3	−3.918	−3.923
Sc–Au	*CO	−0.619	−0.638
Sc–Au	*H	0.083	0.088
Sc–Pd	*OCH_2CH_3	−3.851	−3.928
Sc–Pd	*CO	−0.450	−0.421
Sc–Pd	*H	−0.116	−0.110
Sc–Zn	*OCH_2CH_3	−3.894	−3.850
Sc–Zn	*CO	−0.456	−0.486
Sc–Zn	*H	0.222	0.249
Y–Pd–In	*OCH_2CH_3	−3.677	−3.650
Y–Pd–In	*CO	−0.557	−0.552
Y–Pd–In	*H	−0.018	0.001
Zn–Pd–In	*OCH_2CH_3	−3.699	−3.707
Zn–Pd–In	*CO	−0.811	−0.807
Zn–Pd–In	*H	0.071	0.080

Supplementary Table 7. Energy differences between the final and initial states for five representative CO–CO coupling pathways.

Representative candidates	ΔE (eV)
Ga–Pt	0.453
Sc–Cu–Ga	1.347
Cu–Pd–Sn	1.825
Cu	0.945
Al–Cu–Pd	0.436

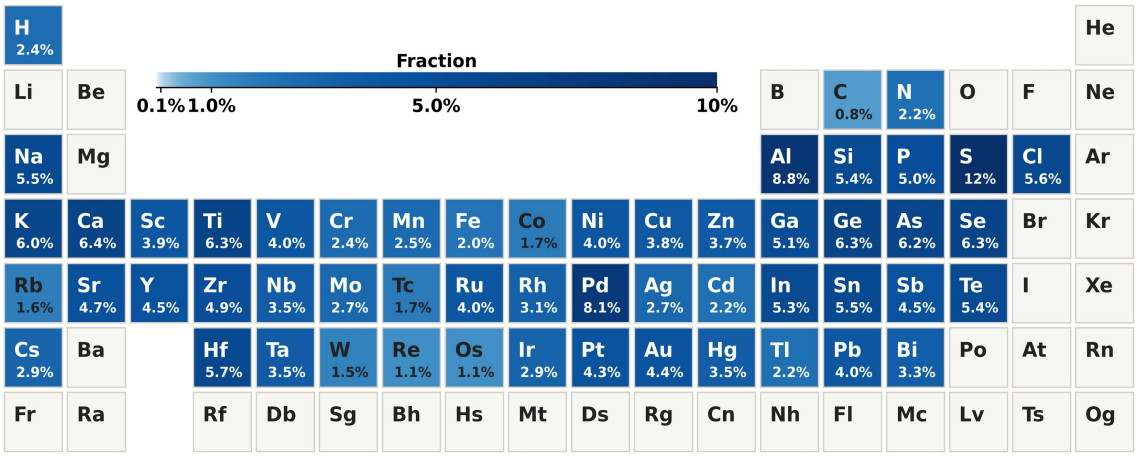

Supplementary Figure 1. Elemental distribution of the fine-tuning dataset. The percentage shown for each element is the fraction of the 14,000 fine-tuning structures containing at least one slab atom of that element.

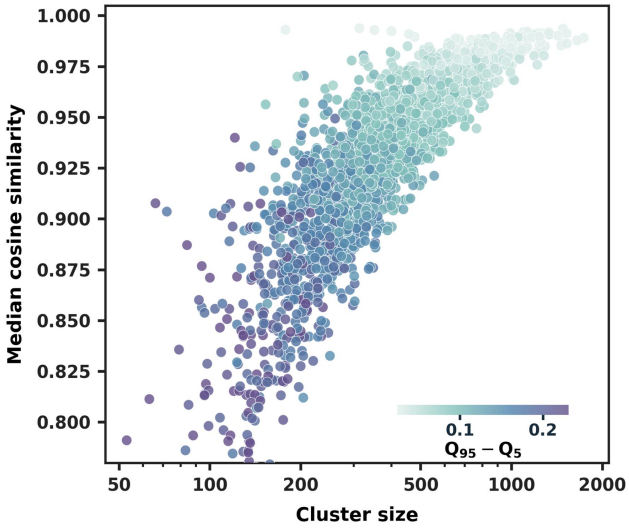

Supplementary Figure 2. Population and compactness of the O-centered embedding clusters. Each point represents one of the 2,000 spherical k-means clusters. Cluster size is plotted against the median cosine similarity between member embeddings and the corresponding cluster centroid. Color denotes the 5th-to-95th-percentile range, Q_{95} - Q_5, of the within-cluster cosine similarities.

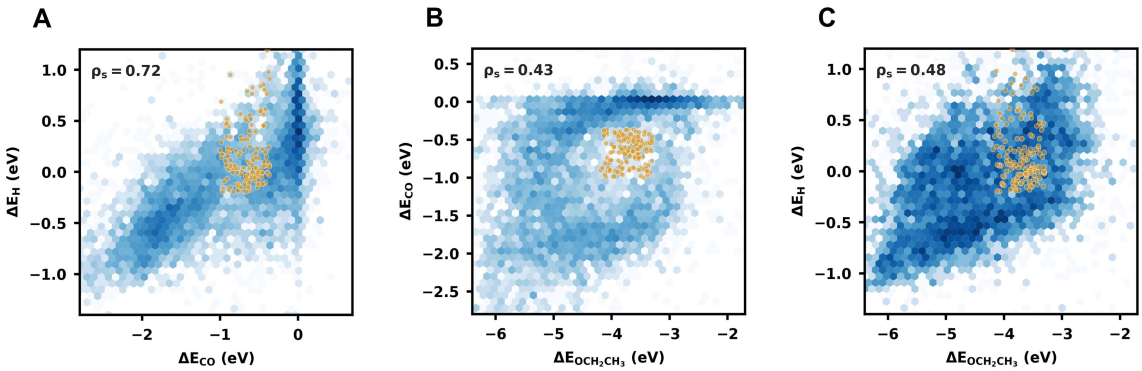

Supplementary Figure 3. Pairwise relationships among the UMA-predicted adsorption energies derived from the 10,000 representative structures. The analysis includes structures for which the *OCH_2CH_3, *CO, and *H relaxations all converged. Hexagonal-bin intensity represents local structure density, and gold points denote the 153 structures satisfying all three adsorption-energy criteria. (A) *CO versus *H. (B) *OCH_2CH_3 versus *CO. (C) *OCH_2CH_3 versus *H. The Spearman rank correlation coefficient is reported in each panel.

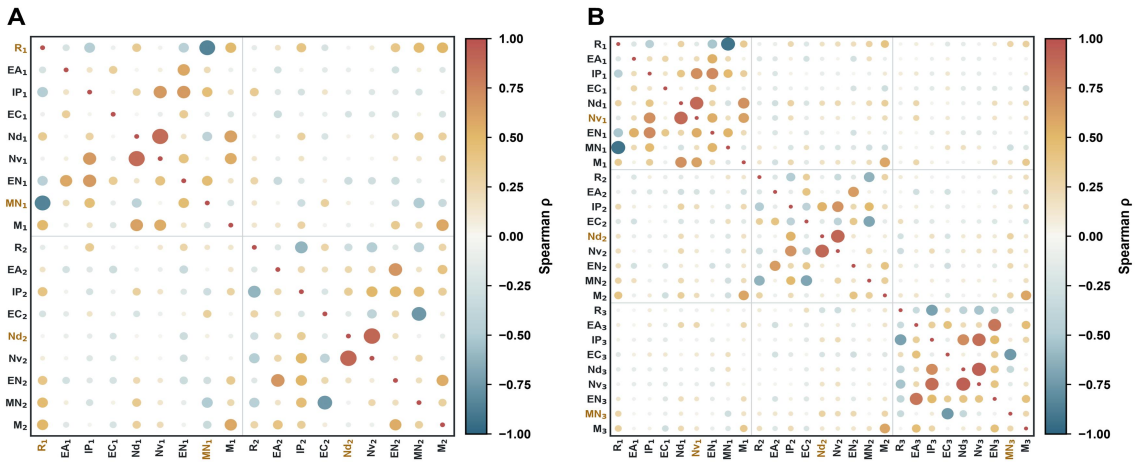

Supplementary Figure 4. Spearman correlations among elemental descriptors used for subgroup discovery. Correlation matrices are shown for (A) binary and (B) ternary structures. Circle color and size represent the sign and magnitude of the correlation coefficient, respectively. Gold labels denote descriptors included in the highest-ranked subgroup rules.

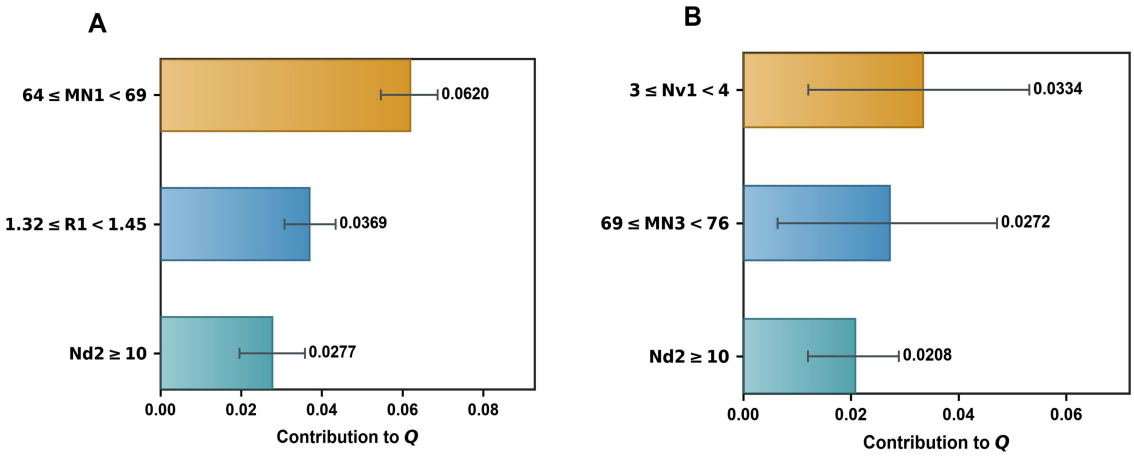

Supplementary Figure 5. Condition-level attribution of the highest-ranked subgroup rules. Shapley contributions to the StandardQF quality score *Q* are shown for the binary rule (A) and ternary rule (B). Numerical labels give the contribution of each condition, and error bars represent 95% confidence intervals obtained from 2,000 nonparametric bootstrap resamples. For each rule, the condition-level contributions sum to the quality score of the complete rule.

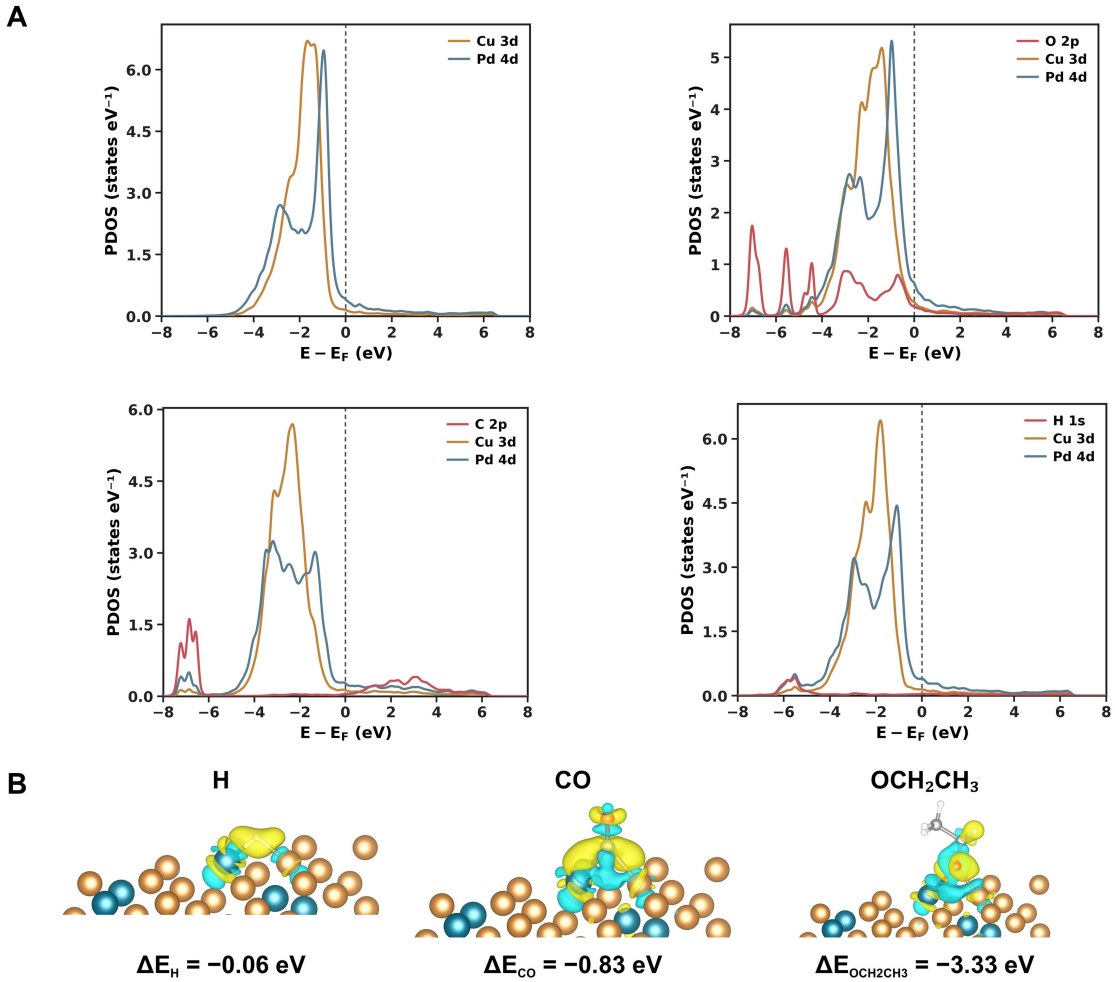

Supplementary Figure 6. Electronic-structure analysis of a representative rule-matching Cu-Pd system. (A) PDOS of the clean surface and the corresponding *H-, *CO-, and *OCH_2CH_3-adsorbed configurations. (B) Adsorption-induced charge-density differences for *H, *CO, and *OCH_2CH_3. Yellow and cyan isosurfaces indicate electron accumulation and depletion, respectively, at an isovalue of 0.003 e $bohr^{-3}$.

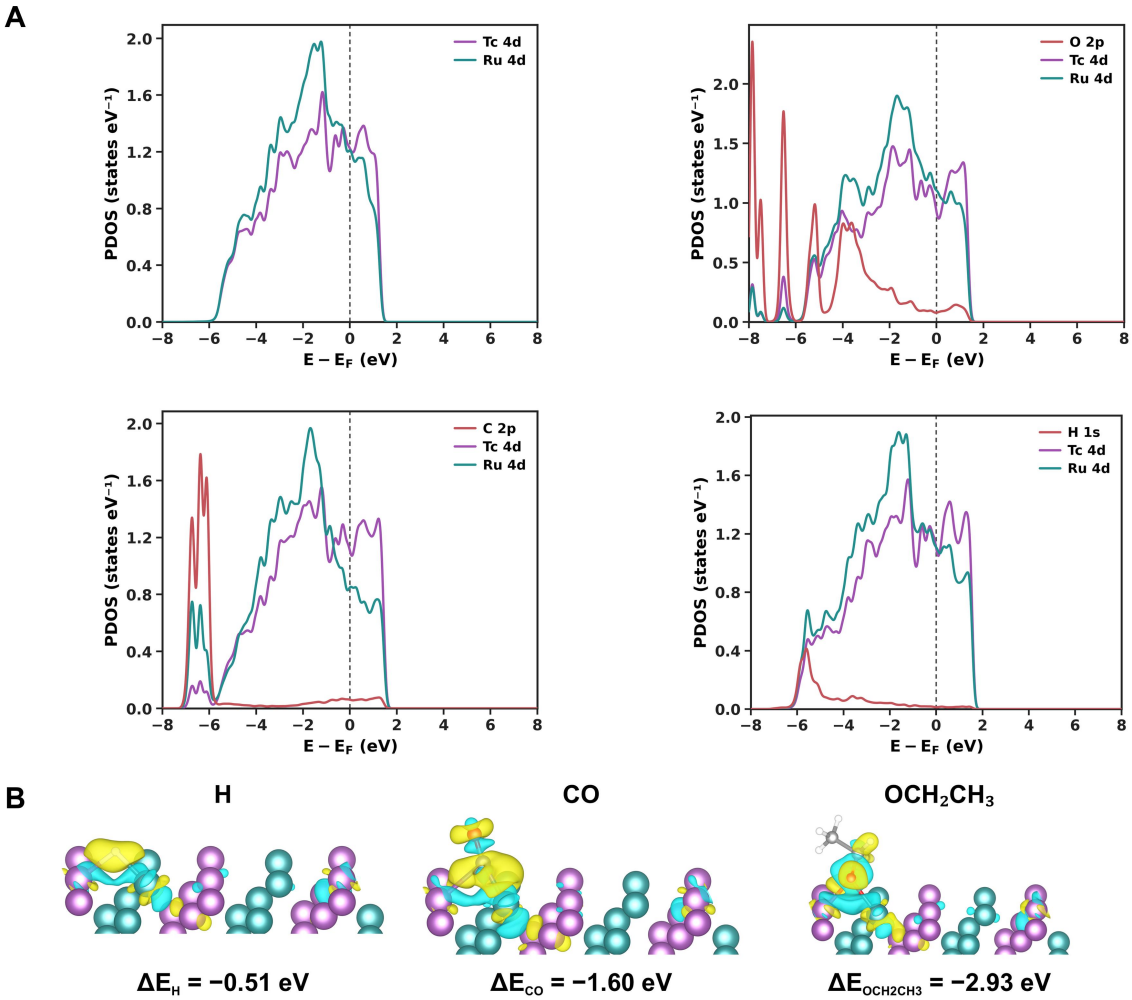

Supplementary Figure 7. Electronic-structure analysis of a representative rule-mismatching Tc-Ru system. (A) PDOS of the clean surface and the corresponding *H-, *CO-, and *OCH_2CH_3-adsorbed configurations. (B) Adsorption-induced charge-density differences for *H, *CO, and *OCH_2CH_3. Yellow and cyan isosurfaces indicate electron accumulation and depletion, respectively, at an isovalue of 0.003 e $bohr^{-3}$.

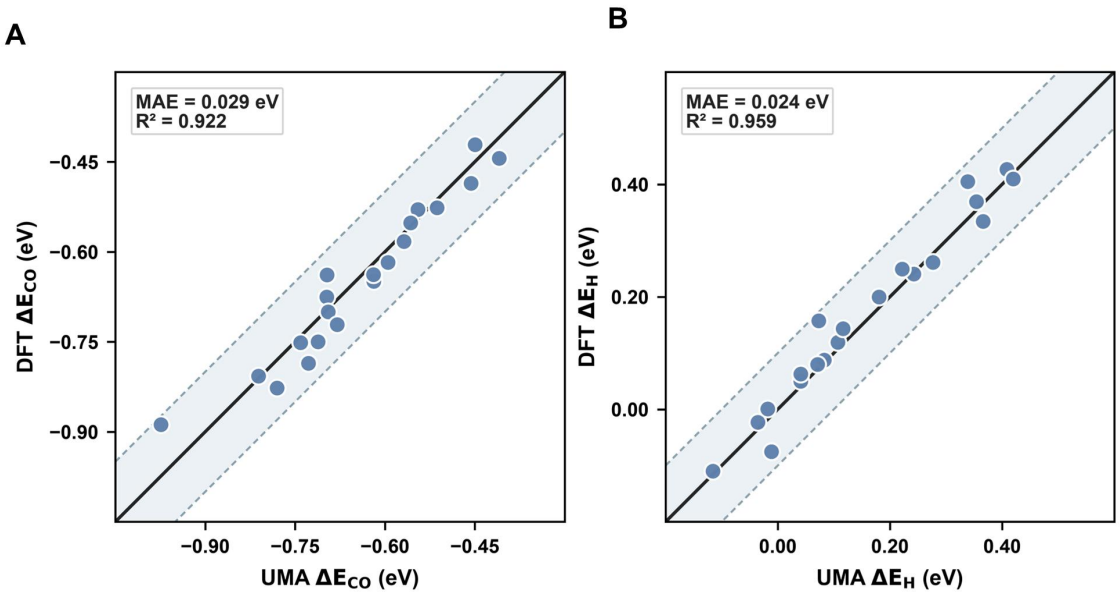

Supplementary Figure 8. Agreement between UMA- and DFT-derived adsorption energies. UMA adsorption energies are compared with the corresponding DFT values for *CO (A) and *H (B) across 20 DFT-validated candidate systems. The solid diagonal denotes exact agreement, and the shaded region bounded by dashed lines indicates deviations within ±0.10 eV. The mean absolute error (MAE) and coefficient of determination (R^2) are reported in each panel.

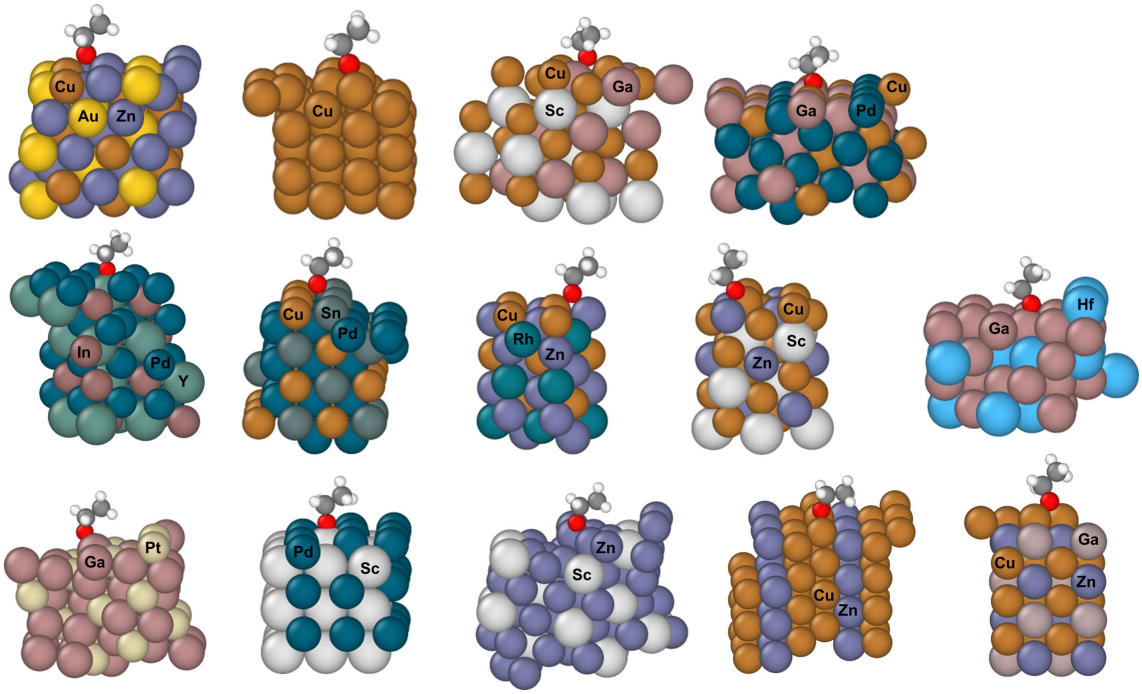

Supplementary Figure 9. Representative DFT-optimized adsorption structures for *OCH_2CH_3.

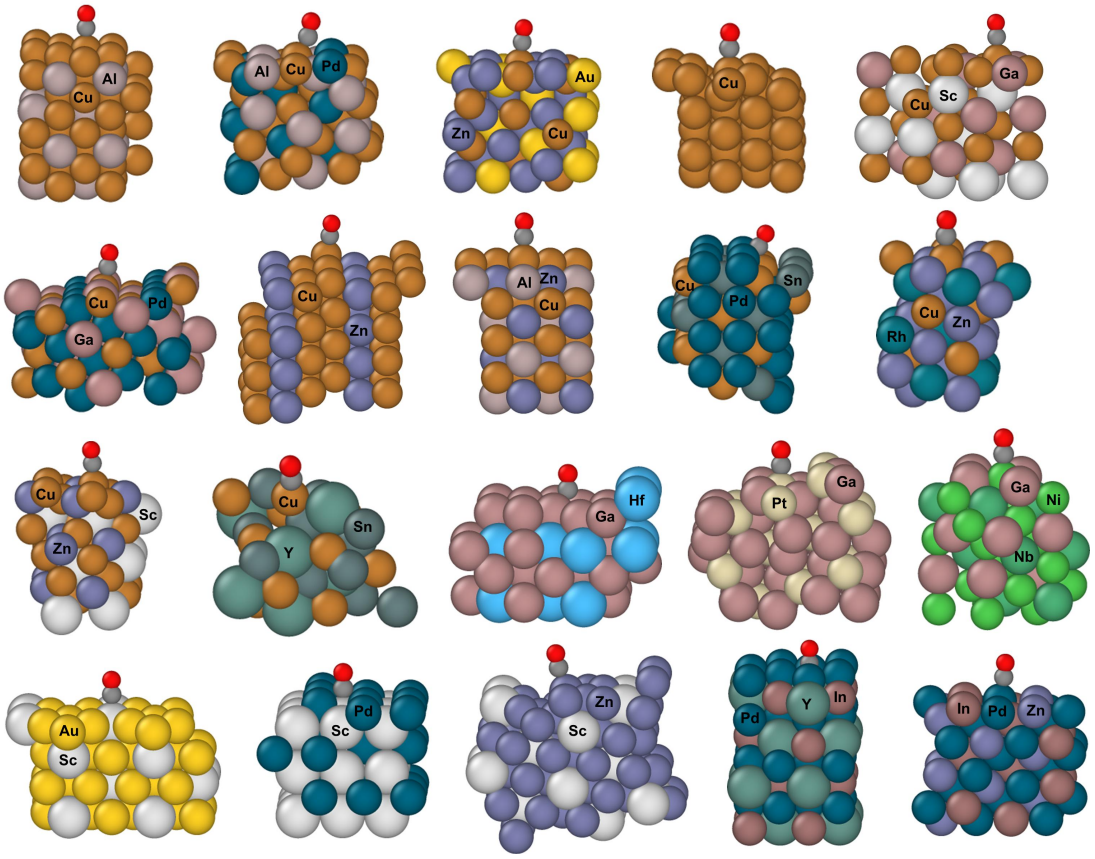

Supplementary Figure 10. Representative DFT-optimized adsorption structures for *CO.

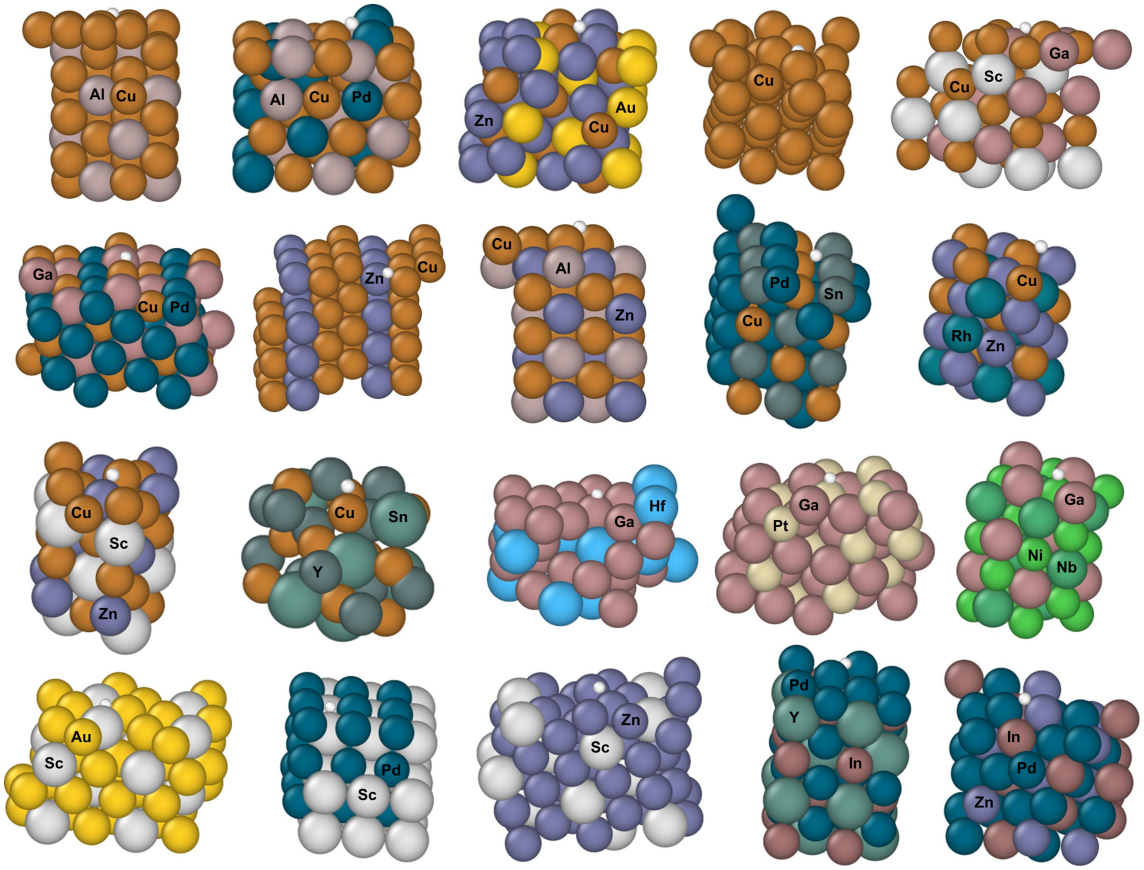

Supplementary Figure 11. Representative DFT-optimized adsorption structures for *H.

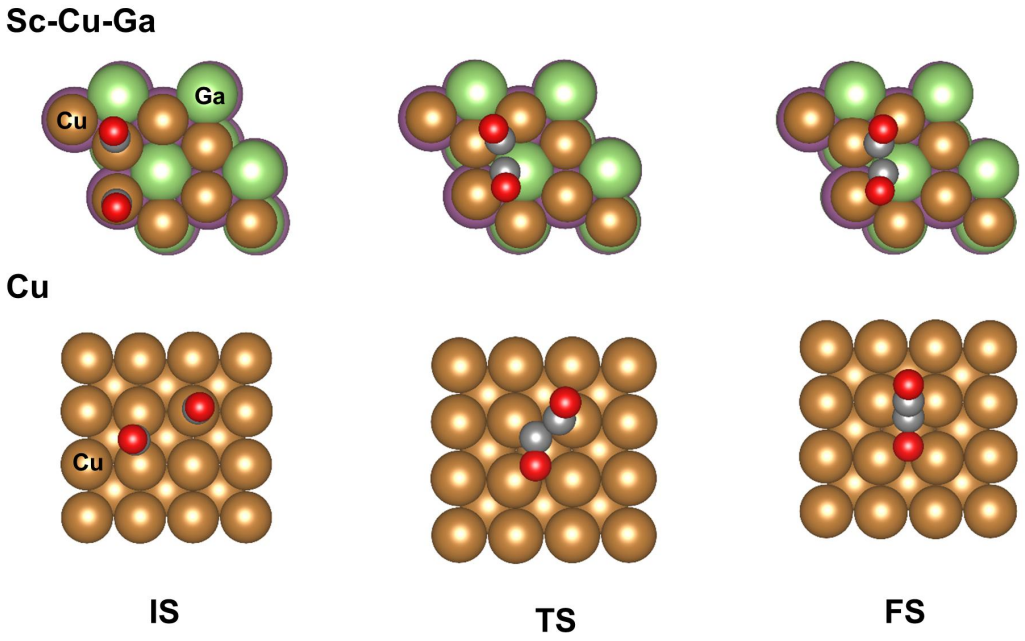

Supplementary Figure 12. Initial-state (IS), transition-state (TS), and final-state (FS) structures for representative Sc-Cu-Ga and Cu systems. From left to right, the columns correspond to IS, TS, and FS, respectively.

REFERENCES

[1] Chanussot, L.; Das, A.; Goyal, S.; et al. Open Catalyst 2020 (OC20) dataset and community challenges. *ACS Catal.* **2021**, *11*, 6059-6072. DOI: 10.1021/acscatal.0c04525

[2] Wood, B. M.; Dzamba, M.; Fu, X.; et al. UMA: a family of universal models for atoms. *Adv. Neural Inf. Process. Syst.* **2025**, *38*, 129391-129427. DOI: 10.52202/085713-4310

[3] Kresse, G.; Furthmüller, J. Efficiency of ab-initio total energy calculations for metals and semiconductors using a plane-wave basis set. *Comput. Mater. Sci.* **1996**, *6*, 15-50. DOI: 10.1016/0927-0256(96)00008-0

[4] Kresse, G.; Furthmüller, J. Efficient iterative schemes for ab initio total-energy calculations using a plane-wave basis set. *Phys. Rev. B* **1996**, *54*, 11169-11186. DOI: 10.1103/PhysRevB.54.11169

[5] Hammer, B.; Hansen, L. B.; Nørskov, J. K. Improved adsorption energetics within density-functional theory using revised Perdew-Burke-Ernzerhof functionals. *Phys. Rev. B* **1999**, *59*, 7413-7421. DOI: 10.1103/PhysRevB.59.7413

[6] Kresse, G.; Joubert, D. From ultrasoft pseudopotentials to the projector augmented-wave method. *Phys. Rev. B* **1999**, *59*, 1758-1775. DOI: 10.1103/PhysRevB.59.1758

[7] Henkelman, G.; Jónsson, H. A dimer method for finding saddle points on high dimensional potential surfaces using only first derivatives. *J. Chem. Phys.* **1999**, *111*, 7010-7022. DOI: 10.1063/1.480097

[8] Heyden, A.; Bell, A. T.; Keil, F. J. Efficient methods for finding transition states in chemical reactions: comparison of improved dimer method and partitioned rational function optimization method. *J. Chem. Phys.* **2005**, *123*, 224101. DOI: 10.1063/1.2104507

[9] Blöchl, P. E.; Jepsen, O.; Andersen, O. K. Improved tetrahedron method for Brillouin-zone integrations. *Phys. Rev. B* **1994**, *49*, 16223-16233. DOI: 10.1103/PhysRevB.49.16223

[10] Momma, K.; Izumi, F. VESTA 3 for three-dimensional visualization of crystal, volumetric and morphology data. *J. Appl. Crystallogr.* **2011**, *44*, 1272-1276. DOI: 10.1107/S0021889811038970

[11] Johnson, J.; Douze, M.; Jégou, H. Billion-scale similarity search with GPUs. *IEEE Trans. Big Data* **2021**, *7*, 535-547. DOI: 10.1109/TBDATA.2019.2921572

[12] Ong, S. P.; Richards, W. D.; Jain, A.; et al. Python Materials Genomics (pymatgen): a robust, open-source Python library for materials analysis. *Comput. Mater. Sci.* **2013**, *68*, 314-319. DOI: 10.1016/j.commatsci.2012.10.028

[13] Atzmueller, M. Subgroup discovery. *WIREs Data Min. Knowl. Discov.* **2015**, *5*, 35-49. DOI: 10.1002/widm.1144

[14] Lemmerich, F.; Becker, M. pysubgroup: easy-to-use subgroup discovery in Python. In *Machine Learning and Knowledge Discovery in Databases: European Conference, ECML PKDD 2018, Dublin, Ireland, September 10–14, 2018, Proceedings, Part III*; Brefeld, U.; Curry, E.; Daly, E.; MacNamee, B.; Marascu, A.; Pinelli, F.; Berlingerio, M.; Hurley, N., Eds.; Lecture Notes in Computer Science, Vol. 11053; Springer: Cham, Switzerland, 2019; pp 658-662. DOI: 10.1007/978-3-030-10997-4_46

[15] Shapley, L. S. A value for n-person games. In *Contributions to the Theory of Games, Vol. II*; Kuhn, H. W.; Tucker, A. W., Eds.; Annals of Mathematics Studies, Vol. 28; Princeton University Press: Princeton, NJ, 1953; pp 307-318. DOI: 10.1515/9781400881970-018

[16] Arul Dhas, N.; Paul Raj, C.; Gedanken, A. Synthesis, characterization, and properties of metallic copper nanoparticles. *Chem. Mater.* **1998**, *10*, 1446-1452. DOI: 10.1021/cm9708269

[17] Alam, S. N.; Shrivastava, P.; Panda, D.; Gunale, B.; Susmitha, K.; Pola, P. Synthesis of Al_2Cu intermetallic compound by mechanical alloying. *Mater. Today Commun.* **2022**, *31*, 103267. DOI: 10.1016/j.mtcomm.2022.103267

[18] Chen, Z.; Hou, Y.; Xie, B.; Zhang, Q. Dendrite morphology evolution of Al_6Mn phase in suction casting Al-Mn alloys. *Materials* **2020**, *13*, 2388. DOI: 10.3390/ma13102388

[19] Khoudiakov, M.; Ellis, A. B.; Perepezko, J. H.; Kim, S.; Kepler, K. D. Low-temperature, mercury-mediated synthesis of aluminum intermetallics. *Chem. Mater.* **2000**, *12*, 2008-2013. DOI: 10.1021/cm0000245

[20] Barrios Jiménez, A. M.; Sichevych, O.; Spanos, I.; Altendorf, S. G.; Ormeci, A.; Antonyshyn, I. Al-Pt compounds catalyzing the oxygen evolution reaction. *Dalton Trans.* **2023**, *52*, 1433-1440. DOI: 10.1039/D2DT03234A

[21] Deller, K.; Eisenmann, B. Zur Kenntnis von $Ca_{11}Sb_{10}$ und $Ca_{11}Bi_{10}$. *Z. Naturforsch. B* **1976**, *31*, 29-34. DOI: 10.1515/znb-1976-0105

[22] Bruzzone, G. The binary systems calcium-copper, strontium-copper and barium-copper. *J. Less-Common Met.* **1971**, *25*, 361-366. DOI: 10.1016/0022-5088(71)90178-0

[23] Ding, K.; Qu, R.; Zhou, L.; et al. In situ preparation of CuCl cubic particles on the commercial copper foil: its significant facilitation to the electrochemical performance of the commercial graphite and its unexpected photochromic behavior. *J. Alloys Compd.* **2020**, *835*, 155302. DOI: 10.1016/j.jallcom.2020.155302

[24] Gupta, S. P. Kinetics of discontinuous precipitation and dissolution in Cu-Ag alloys. *Can. Metall. Q.* **1998**, *37*, 141-159. DOI: 10.1016/S0008-4433(98)00014-7

[25] Markovic, I.; Nestorovic, S.; Markovic, D. Effect of thermo-mechanical treatment on properties improvement and microstructure changes in copper-gold alloy. *Mater. Des.* **2014**, *53*, 137-144. DOI: 10.1016/j.matdes.2013.06.062

[26] Nazarian-Samani, M.; Abdollah-Pour, H.; Mirzaee, O.; Kamali, A. R.; Nazarian-Samani, M. Effects of Ni addition on the microstructure and properties of nanostructured copper-germanium alloys. *Intermetallics* **2013**, *38*, 80-87. DOI: 10.1016/j.intermet.2013.02.015

[27] Saravanan, G.; Khobragade, R.; Nagar, L. C.; Labhsetwar, N. Ordered intermetallic Pt-Cu nanoparticles for the catalytic CO oxidation reaction. *RSC Adv.* **2016**, *6*, 85634-85642. DOI: 10.1039/C6RA19602K

[28] Halimi, R.; Hamana, D.; Chpilevski, E. M. Réaction à l'état solide dans les couches minces du système binaire Cu/Sb. *Thin Solid Films* **1986**, *139*, 147-155. DOI: 10.1016/0040-6090(86)90333-0

[29] Dashevskyi, M.; Belyavina, N. M.; Boshko, O.; Kapitanchuk, L.; Nakonechna, O.; Revo, S. On the features of mechanochemical synthesis of Y-Cu equiatomic powder mixture. *Adv. Powder Technol.* **2018**, *29*, 1106-1111. DOI: 10.1016/j.apt.2018.01.029

[30] Wang, Y.; Hall, A. S. Room-temperature synthesis of intermetallic Cu-Zn by an electrochemically induced phase transformation. *Chem. Mater.* **2021**, *33*, 7309-7314. DOI: 10.1021/acs.chemmater.1c01678

[31] Pötzschke, M.; Schubert, K. Zum Aufbau einiger zu T4-B3 homologer und quasihomologer Systeme. I. Die Systeme Titan-Gallium, Zirkonium-Gallium und Hafnium-Gallium. *Z. Metallkd.* **1962**, *53*, 474-488. DOI: 10.1515/ijmr-1962-530708

[32] Tillard, M.; Belin, C. The new intermetallic compound Ga_5Pt: structure from a twinned crystal. *Intermetallics* **2011**, *19*, 518-525. DOI: 10.1016/j.intermet.2010.11.031

[33] Gürler, R.; Pratt, J. N. Some constitutional studies on the molybdenum-rhodium system. *J. Alloys Compd.* **1991**, *177*, 321-330. DOI: 10.1016/0925-8388(91)90085-A

[34] Huang, D.; Niu, C.; Yan, B.; et al. Synthesis of manganese mononitride with tetragonal structure under pressure. *Crystals* **2019**, *9*, 511. DOI: 10.3390/cryst9100511

[35] de Souza, E. F.; Chagas, C. A.; Ramalho, T. C.; de Alencastro, R. B. A versatile low temperature solid-state synthesis of vanadium nitride (VN) via a “guanidinium-route”: experimental and theoretical studies from the key-intermediate to the final product. *Dalton Trans.* **2012**, *41*, 14381-14390. DOI: 10.1039/C2DT31614E

[36] Liu, J.; Yu, X.; Du, R.; et al. Chromium phosphide CrP as highly active and stable electrocatalysts for oxygen electroreduction in alkaline media. *Appl. Catal. B Environ.* **2019**, *256*, 117846. DOI: 10.1016/j.apcatb.2019.117846

[37] Parthé, E.; Parthé, E. Note on the structure of ScP and YP. *Acta Crystallogr.* **1963**, *16*, 71. DOI: 10.1107/S0365110X63000141

[38] Pöttgen, R. Preparation, crystal structure and properties of $RuIn_3$. *J. Alloys Compd.* **1995**, *226*, 59-64. DOI: 10.1016/0925-8388(95)01575-2

[39] Fukuoka, H.; Kawata, N.; Furuta, M.; Katakami, Y.; Kimura, S.; Inumaru, K. High-pressure synthesis and crystal structure of the sulfur-richest chromium sulfide CrS_3 composed of Cr(III) and disulfide ions. *Inorg. Chem.* **2020**, *59*, 13320-13325. DOI: 10.1021/acs.inorgchem.0c01690

[40] Kundu, J.; Pradhan, D. Influence of precursor concentration, surfactant and temperature on the hydrothermal synthesis of CuS: structural, thermal and optical properties. *New J. Chem.* **2013**, *37*, 1470-1478. DOI: 10.1039/C3NJ41142G

[41] Salavati-Niasari, M.; Banaiean-Monfared, G.; Emadi, H.; Enhessari, M. Synthesis and characterization of nickel sulfide nanoparticles via cyclic microwave radiation. *C. R. Chim.* **2013**, *16*, 929-936. DOI: 10.1016/j.crci.2013.01.011

[42] Paca, A. M.; Ajibade, P. A. Bis-(N-ethylphenyldithiocarbamato)palladium(II) as molecular precursor for palladium sulfide nanoparticles. *J. Mol. Struct.* **2021**, *1243*, 130777. DOI: 10.1016/j.molstruc.2021.130777

[43] Palenzona, A.; Manfrinetti, P. The phase diagram of the Sc-Au system. *J. Alloys Compd.* **1997**, *257*, 224-226. DOI: 10.1016/S0925-8388(97)00022-4

[44] Kotur, B.; Derkach, V. O.; Dutsyak, I. S.; Pavlyshyn, A. Z. Structure and electrical properties of $ScCu_4$ as bulk alloy and thin film. *J. Alloys Compd.* **1996**, *238*, 81-85. DOI: 10.1016/0925-8388(95)02162-0

[45] Palenzona, A.; Manfrinetti, P.; Palenzona, R. A reinvestigation of the Sc-In system and related (Tm,Lu)-In compounds. *J. Alloys Compd.* **1996**, *243*, 182-185. DOI: 10.1016/S0925-8388(96)02402-4

[46] Solokha, P.; Eremin, R. A.; Leisegang, T.; et al. New quasicrystal approximant in the Sc-Pd system: from topological data mining to the bench. *Chem. Mater.* **2020**, *32*, 1064-1079. DOI: 10.1021/acs.chemmater.9b03767

[47] Liu, X.; Rau, F.; Breu, J.; Range, K. J. Studies on AB2-type intermetallic compounds, IV. High-pressure synthesis and crystal structure of scandium dizinc $ScZn_2$. *J. Alloys Compd.* **1996**, *243*, L5-L7. DOI: 10.1016/S0925-8388(96)02368-7

[48] Corrêa, C. A.; Poupon, M.; Kopeček, J.; et al. Phase transitions of $Cu_{3+x}Si$ observed by temperature-dependent X-ray powder diffraction. *Intermetallics* **2017**, *91*, 129-139. DOI: 10.1016/j.intermet.2017.07.003

[49] Lee, W.; Lee, J.; Bae, J. D.; Byun, C. S.; Kim, D. K. Syntheses of Ni_2Si, Ni_5Si_2, and NiSi by mechanical alloying. *Scr. Mater.* **2001**, *44*, 97-103. DOI: 10.1016/S1359-6462(00)00547-9

[50] Conrad, M.; Harbrecht, B. Synthesis of tantalum tellurides: the crystal structure of Ta_2Te_3. *J. Alloys Compd.* **1992**, *187*, 181-192. DOI: 10.1016/0925-8388(92)90532-E

[51] Wodniecki, P.; Wodniecka, B.; Kulińska, A.; Uhrmacher, M.; Lieb, K. P. The $TiPd_2$ compound studied by PAC with 181Ta and 111Cd probes. *J. Alloys Compd.* **2004**, *385*, 53-58. DOI: 10.1016/j.jallcom.2004.04.121

[52] Bronsema, K. D.; Bus, G. W.; Wiegers, G. A. The crystal structure of vanadium ditelluride, $V_{1+x}Te_2$. *J. Solid State Chem.* **1984**, *53*, 415-421. DOI: 10.1016/0022-4596(84)90120-8

[53] Luo, Y.; Sun, Y.; Schwarz, U.; Armbrüster, M. Systematic exploration of synthesis pathways to nanoparticulate ZnPd. *Chem. Mater.* **2012**, *24*, 3094-3100. DOI: 10.1021/cm3018192

[54] Miura, A.; Wang, H.; Leonard, B. M.; Abruña, H. D.; DiSalvo, F. J. Synthesis of intermetallic PtZn nanoparticles by reaction of Pt nanoparticles with Zn vapor and their application as fuel cell catalysts. *Chem. Mater.* **2009**, *21*, 2661-2667. DOI: 10.1021/cm900048e

[55] Gross, N.; Kotzyba, G.; Künnen, B.; Jeitschko, W. Binary compounds of rhodium and zinc: RhZn, Rh_2Zn_{11}, and $RhZn_{13}$. *Z. Anorg. Allg. Chem.* **2001**, *627*, 155-163. DOI: 10.1002/1521-3749(200102)627:2<155::AID-ZAAC155>3.0.CO;2-C

[56] Lim, A. B. Y.; Long, X.; Shen, L.; et al. Effect of palladium on the mechanical properties of Cu-Al intermetallic compounds. *J. Alloys Compd.* **2015**, *628*, 107-112. DOI: 10.1016/j.jallcom.2014.12.119

[57] Zobac, O.; Kroupa, A.; Richter, K. W. Experimental study of the Al-Cu-Zn ternary phase diagram. *J. Mater. Sci.* **2020**, *55*, 10796-10810. DOI: 10.1007/s10853-020-04686-4

[58] Feng, Q.; Nandy, T. K.; Tryon, B.; Pollock, T. M. Deformation of Ru-Al-Ta ternary alloys. *Intermetallics* **2004**, *12*, 755-762. DOI: 10.1016/j.intermet.2004.02.016

[59] Kubitza, N.; Reitz, A.; Zieschang, A.-M.; et al. From MAX phase carbides to nitrides: synthesis of V_2GaC, V_2GaN, and the carbonitride $V_2GaC_{1-x}Nx$. *Inorg. Chem.* **2022**, *61*, 10634-10641. DOI: 10.1021/acs.inorgchem.2c00200

[60] Zhao, X.; Zhang, H.; Yan, Y.; et al. Engineering the electrical conductivity of lamellar silver-doped cobalt(II) selenide nanobelts for enhanced oxygen evolution. *Angew. Chem. Int. Ed.* **2017**, *56*, 328-332. DOI: 10.1002/anie.201609080

[61] Hisatsune, K.; Baba, K.; Hasaka, M.; et al. Phase transformation in a dental Pd-Cu-Ga alloy. *J. Alloys Compd.* **1995**, *230*, 94-99. DOI: 10.1016/0925-8388(95)01695-3

[62] Su, J.; Feng, J.; Feng, Y.; et al. Single-site Cu-doped PdSn wavy nanowires for highly active, stable, and CO-tolerant ethanol oxidation electrocatalysis. *Precis. Chem.* **2023**, *1*, 363-371. DOI: 10.1021/prechem.3c00055

[63] Li, C.; Wang, L.; Inoue, A. Precipitation of nanoscale icosahedral quasicrystalline phase in Hf-Cu-(Rh, Ir) amorphous alloys. *Eur. Phys. J. Appl. Phys.* **2001**, *16*, 183-186. DOI: 10.1051/epjap:2001208

[64] Sebastian, C. P.; Fehse, C.; Eckert, H.; Hoffmann, R. D.; Pöttgen, R. Structure, ^{119}Sn solid-state NMR and Mössbauer spectroscopy of RECuSn (RE = Sc, Y, La, Lu). *Solid State Sci.* **2006**, *8*, 1386-1392. DOI: 10.1016/j.solidstatesciences.2006.07.006

[65] Seol, H. J.; Shiraishi, T.; Tanaka, Y.; Miura, E.; Hisatsune, K.; Kim, H. I. Ordering behaviors and age-hardening in experimental AuCu-Zn pseudobinary alloys for dental applications. *Biomaterials* **2002**, *23*, 4873-4879. DOI: 10.1016/S0142-9612(02)00245-4

[66] Kwon, T.; Jun, M.; Bang, G. J.; et al. Dopant-assisted control of the crystallite domain size in hollow ternary iridium alloy octahedral nanocages toward the oxygen evolution reaction. *Cell Rep. Phys. Sci.* **2020**, *1*, 100260. DOI: 10.1016/j.xcrp.2020.100260

[67] Sijpkes, A. H.; van der Puil, N.; van den Brink, P. J.; de Keijzer, A. H. J. F.; Abdul Hamid, S. B. Chromium-free catalysts of metalic Cu and at least one second metal. WO 2005070537A1, 2005.

[68] Babizhetskyy, V.; Myakush, O.; Kotur, B.; Smetana, V.; Zheng, C.; Mudring, A.-V. Crystal and electronic structures of the new ternary gallide $Zr_{12}Pd_{40-x}Ga_{31+y}$ (x = 0-1.5, y = 0-0.5). *J. Solid State Chem.* **2023**, *327*, 124250. DOI: 10.1016/j.jssc.2023.124250

[69] Eisenmann, B.; Savelsberg, G.; Schäfer, H. Zur Darstellung und Kristallstruktur von Na_2CuAs, K_2CuAs und K_2CuSb. *Z. Naturforsch. B* **1976**, *31*, 1344-1346. DOI: 10.1515/znb-1976-1010

[70] Onwunyiriuwa, G. M.; Nnanna, L. A.; Akpu, N. I.; Ahameful, Y. C.; Akpu, M. O. Impact of yttrium dopant on physical properties of manganese selenide nanoparticles synthesized via spray pyrolysis for photovoltaic applications. *Physics Access* **2025**, *5*, 49-56. DOI: 10.47514/phyaccess.2025.5.1.005

[71] Vennos, D. A.; Badding, M. E.; DiSalvo, F. J. Synthesis, structure, and properties of a new ternary metal nitride, Ca_3CrN_3. *Inorg. Chem.* **1990**, *29*, 4059-4062. DOI: 10.1021/ic00345a030

[72] Maunaye, M.; Guyader, J.; Laurent, Y.; Lang, J. Étude structurale de $CaGeN_2$ et $Ca_{1-x}GeN_2$. *Bull. Soc. Fr. Minéral. Cristallogr.* **1971**, *94*, 347-352. DOI: 10.3406/bulmi.1971.6588

[73] Jin, Z. J.; Liu, C.; Yu, L.; Wu, W. T. Corrosion performance of ion-plated titanium and yttrium-modified TiN coatings. *Surf. Coat. Technol.* **1991**, *46*, 307-315. DOI: 10.1016/0257-8972(91)90173-T

[74] Waki, S.; Yamaguchi, Y.; Mitsugi, K. Superconductivity of Ni_2NbX (X = Al, Ga and Sn). *J. Phys. Soc. Jpn.* **1985**, *54*, 1673-1676. DOI: 10.1143/JPSJ.54.1673

[75] Johrendt, D.; Miericke, R.; Mewis, A. Neue Pnictide mit modifizierten AlB_2-Strukturen / New pnictides with modified AlB_2-type structures. *Z. Naturforsch. B* **1996**, *51*, 905-906. DOI: 10.1515/znb-1996-0625

[76] Lu, A.-Y.; Zhu, H.; Xiao, J.; et al. Janus monolayers of transition metal dichalcogenides. *Nat. Nanotechnol.* **2017**, *12*, 744-749. DOI: 10.1038/nnano.2017.100

[77] Markiv, V. Ya.; Belyavina, N. N.; Gavrilenko, I. S. Crystal structure and some ternary compounds in the system Sc-Cu-Ga. *Izv. Akad. Nauk SSSR, Met.* **1984**, *1984*, 215-217.

[78] Wu, D.; Yang, Y.; Dai, C.; Cheng, D. Enhanced oxygen reduction activity of PtCu nanoparticles by morphology tuning and transition-metal doping. *Int. J. Hydrogen Energy* **2020**, *45*, 4427-4434. DOI: 10.1016/j.ijhydene.2019.12.003

[79] Lin, Q.; Corbett, J. D. New stable icosahedral quasicrystalline phase in the Sc-Cu-Zn system. *Philos. Mag. Lett.* **2003**, *83*, 755-762. DOI: 10.1080/09500830310001614496

[80] Kim, D.-H.; Lee, E.; Pak, C. Effect of rare-earth elements in Pd ternary alloy catalysts on activity toward oxygen reduction reaction. *Catal. Today* **2021**, *359*, 106-111. DOI: 10.1016/j.cattod.2019.12.022

[81] Espinosa, G. P.; Cooper, A. S.; Barz, H. Isomorphs of the superconducting/magnetic ternary stannides. *Mater. Res. Bull.* **1982**, *17*, 963-969. DOI: 10.1016/0025-5408(82)90121-0

[82] Wang, C. P.; Tao, G. M.; Xu, W.; Liu, X. J. Experimental investigation of phase equilibria in the Co-Si-Zr ternary system. *J. Alloys Compd.* **2013**, *574*, 33-40. DOI: 10.1016/j.jallcom.2013.03.179

[83] Kotur, B. Ya.; Gladyshevskii, E. I.; Sikirica, M. A note on the crystal structure of two ScCuSi phases. *J. Less-Common Met.* **1981**, *81*, 71-78. DOI: 10.1016/0022-5088(81)90270-8

[84] Belan, B.; Sojka, L.; Demchyna, M.; Manyako, M.; Kalychak, Y. Synthesis and crystal structures of the new indides Dy_5Pd_2In and Y_5Pd_2In. *Chem. Met. Alloys* **2016**, *9*, 21-26. DOI: 10.30970/cma9.0317

[85] Kushida, Y.; Katagiri, M.; Ikoma, H.; Hirose, S.; Hiramatsu, Y.; Yoneoka, M. Process for producing hydrogen-containing gas. EP 1312413A2, 2003.

[86] Jana, P. P.; Lidin, S. Structural impact of platinum on the incommensurably modulated γ-brass related composite structure $Pd_{15}Zn_{54}$. *Inorg. Chem.* **2012**, *51*, 9893-9901. DOI: 10.1021/ic301326p

[87] Mishra, T.; Heymann, G.; Huppertz, H.; Pöttgen, R. Dimorphism in the REPdZn series. *Intermetallics* **2012**, *20*, 110-114. DOI: 10.1016/j.intermet.2011.08.012

[88] Jain, A.; Ong, S. P.; Hautier, G.; et al. Commentary: the Materials Project: a materials genome approach to accelerating materials innovation. *APL Mater.* **2013**, *1*, 011002. DOI: 10.1063/1.4812323